
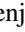










Revisiting Orbital Evolution in HAT-P-2 b and Confirmation of HAT-P-2 c

Zoë L. de Beurs^{1,7} , Julien de Wit¹ , Alexander Venner² , David Berardo³ , Jared Bryan^{1,8} , Joshua N. Winn⁴ , Benjamin J. Fulton⁵ , and Andrew W. Howard⁶ 

¹ Department of Earth, Atmospheric and Planetary Sciences, Massachusetts Institute of Technology, Cambridge, MA 02139, USA; zdebeurs@mit.edu
² Centre for Astrophysics, University of Southern Queensland, Toowoomba, QLD 4350, Australia
³ Department of Physics and Kavli Institute for Astrophysics and Space Research, Massachusetts Institute of Technology, Cambridge, MA 02139, USA
⁴ Department of Astrophysical Sciences, Princeton University, Princeton, NJ 08544, USA
⁵ Cahill Center for Astronomy & Astrophysics, California Institute of Technology, Pasadena, CA 91125, USA
⁶ Department of Astronomy, California Institute of Technology, Pasadena, CA 91125, USA

Received 2023 May 5; revised 2023 July 28; accepted 2023 August 3; published 2023 September 1

Abstract

One possible formation mechanism for Hot Jupiters is that high-eccentricity gas giants experience tidal interactions with their host star that cause them to lose orbital energy and migrate inwards. We study these types of tidal interactions in an eccentric Hot Jupiter called HAT-P-2 b, which is a system where a long-period companion has been suggested and hints of orbital evolution were detected. Using 5 additional years of radial velocity (RV) measurements, we further investigate these phenomena. We investigated the long-period companion by jointly fitting RVs and Hipparcos-Gaia astrometry and confirmed this long-period companion, significantly narrowed down the range of possible periods ($P_2 = 8500^{+2600}_{-1500}$ days), and determined that it must be a substellar object ($10.7^{+5.2}_{-2.2} M_J$). We also developed a modular pipeline to simultaneously model rapid orbital evolution and the long-period companion. We find that the rate and significance of evolution are highly dependent on the long-period companion modeling choices. In some cases the orbital rates of change reached $de/dt = 3.28^{+1.75}_{-1.72} \times 10^{-3} \text{ yr}^{-1}$, $d\omega/dt = 1.12^\circ \pm 0.22^\circ \text{ yr}^{-1}$, which corresponds to a ~ 321 yr apsidal precession period. In other cases, the data is consistent with $de/dt = 7.67 \pm 18.6 \times 10^{-4} \text{ yr}^{-1}$, $d\omega/dt = 0.76^\circ \pm 0.24^\circ \text{ yr}^{-1}$. The most rapid changes found are significantly larger than the expected relativistic precession rate and could be caused by transient tidal planet–star interactions. To definitively determine the magnitude and significance of potential orbital evolution in HAT-P-2 b, we recommend further monitoring with RVs and precise transit and eclipse timings.

Unified Astronomy Thesaurus concepts: [Star-planet interactions \(2177\)](#); [Orbital evolution \(1178\)](#); [Astrometry \(80\)](#); [Radial velocity \(1332\)](#); [Exoplanets \(498\)](#); [Hot Jupiters \(753\)](#)

Supporting material: machine-readable table

1. Introduction

The role of planet–star interactions in the migration of Hot Jupiters is not well understood. The original discovery of Jupiter-sized planets on short-period orbits (Mayor & Queloz 1995) challenged our theories of solar system formation, and it was proposed that Hot Jupiters must have migrated inward after forming beyond the ice line (Lin et al. 1996). One possible migration mechanism proposed is that high-eccentricity gas giants experience tidal interactions with their host star that cause them to lose orbital energy and migrate to a close-in orbit (Rasio & Ford 1996; Weidenschilling & Marzari 1996; Lin & Ida 1997).

High-eccentricity tidal migration theories often focus on the tides within the planet. However, equilibrium tides (Hut 1981; Eggleton et al. 1998) in the star are accompanied by dynamical tides (Goodman & Dickson 1998; Fuller & Lai 2012) consisting of resonantly excited g-modes, which may result in energy and angular momentum exchanges between the star and orbit that can be several orders of magnitude larger (Witte & Savonije 2002;

Ma & Fuller 2021). The resulting changes in the orbit could impact radial velocity (RV) and photometric observations of a planetary system. Hints of rapid orbital evolution were detected in the HAT-P-2 system, where other signs of strong planet–star interactions have been observed (de Wit et al. 2017).

HAT-P-2 is an F8-type star and hosts an $8.70^{+0.19}_{-0.20} M_J$ mass planet on an eccentric ($e = 0.51023 \pm 0.00042$), short-period ($P = 5.6334675 \pm 0.0000013$ days) orbit. Due to this combination of characteristics, it has been identified as an ideal target for studying planet–star interactions (Jordán & Bakos 2008; Fabrycky & Winn 2009; Levrard et al. 2009; Cowan & Agol 2011; Lewis et al. 2013, 2014; Salz et al. 2016).

Now, we are revisiting this interesting system because the California Planet Search (CPS) team observed HAT-P-2 for an additional 5 yr with the High Resolution Echelle Spectrograph (HIRES), which extends the RV baseline from 9 yr to 14 yr. In addition, we also merged RVs from multiple instruments and increased the number of RVs from 54 to 103 compared to de Wit et al. (2017). With these additional RV measurements, we were able to further investigate whether the hints of rapid orbital evolution appear to persist and can be confirmed. We developed our own modular orbital evolution pipeline that allows for an apples-to-apples comparison between various orbital models.

In addition, we performed an in-depth assessment of the possibility of an outer long-period companion, as has been suggested by Lewis et al. (2013), Knutson et al. (2014),

⁷ NSF Graduate Research Fellow, MIT Presidential Fellow, and MIT Collamore-Rogers Fellow.

⁸ NSF Graduate Research Fellow and MIT Presidential Fellow.



Bonomo et al. (2017), and Ment et al. (2018). We combined our RV measurements with astrometric observations and confirmed a persistent signal caused by a substellar long-period companion, HAT-P-2 c.

Our paper is organized as follows. In Section 2, we describe the RV and astrometric data included in this analysis. In Section 3, we describe the RV orbital fitting pipeline and how we performed a joint astrometric-RV fit. In Section 4, we detail our results and evaluate our models. In Section 5, we give an interpretation of these results. Lastly, in Sections 6 and 7, we provide directions for future work and we conclude.

2. Data

2.1. Precise Radial Velocity Measurements

Our analysis includes 72 spectra of HAT-P-2 obtained by the CPS Team using HIRES on the W.M. Keck Observatory 10 m telescope, Keck I (Vogt et al. 1994). The standard CPS data-reduction pipeline was used, which uses an iodine cell as a wavelength reference, as further described in Howard et al. (2010). These 72 RVs span 14 yr (2006 September 3–2020 August 31). For comparison, de Wit et al. (2017) used 44 HIRES RVs that span 9 yr (2006 September–2015 October).

In addition to our 72 HIRES RVs, we also included 31 publicly available RVs from the HARPS-N spectrograph at the 3.6 m Telescopio Nazionale Galileo on La Palma in the Canary Islands. HARPS-N is a temperature- and pressure-stabilized echelle spectrograph (Cosentino et al. 2012). HARPS-N spans the wavelength range from 383 to 693 nm and has a resolving power of $\lambda/\Delta\lambda = 115,000$. These RVs span 2013 March 12–2017 August 28. We included the published RVs from Bonomo et al. (2017) and downloaded additional publicly available RVs through the TNG Archive.⁹

We removed RV measurements that occur during transit (Winn et al. 2007) such that we are not using RVs which are affected by the Rossiter–McLaughlin effect. The RVs are included in the Appendix in Table A1.

2.2. Astrometric Measurements

The astrometric data used in this work are derived from the Hipparcos-Gaia Catalog of Accelerations (Brandt 2018, 2021). This consists of three independent proper-motion measurements: the Hipparcos proper motion (μ_H), the Gaia Data Release 3 proper motion (μ_G), and the mean Hipparcos-Gaia proper motion (μ_{HG}); see Brandt (2018) and Brandt et al. (2019) for further details. The astrometric data have a time baseline of approximately 25 yr (1991–2016).

RVs provide us with the minimum mass $M_p \sin(i)$ of an object, where i is the inclination of the system. However, when combining RVs with astrometric measurements, we can constrain the inclination of the system and derive the actual mass (M_p). In this way, astrometric measurements can help constrain the nature of the outer companion of HAT-P-2 (stellar, brown dwarf, planet).

3. Data Analysis

3.1. Radial Velocity Orbital Fitting Pipeline

We designed a modular RV orbital fitting pipeline that allows for comparison of various dynamical scenarios to determine the origins of the RV variation seen in de Wit et al. (2017). We use `radvel`'s `kepler.rv_drive` function

(Fulton et al. 2018) to solve Kepler's equation in our pipeline¹⁰ and build upon this software by allowing orbital parameters to change over time. Our modular pipeline is parallelized to speed up orbital fitting and can easily be applied to other RV data sets. Our pipeline can notably perform fits of the following stable orbital configurations: (i) a stable one-planet Keplerian fit, (ii) a stable two-planet Keplerian fit, (iii) a stable two-planet fit where the long-period companion is modeled as a quadratic trend. In addition, our pipeline can model the eccentricity (e) and argument of periastron (ω) as linearly evolving parameters such that $e = de/dt \cdot \text{time} + e_0$ and $\omega = d\omega/dt \cdot \text{time} + \omega_0$. We refer to models where e and ω can linearly evolve with time as first-order, evolving models. In particular, our pipeline can perform the following evolving orbital configurations: (iv) a first-order, evolving one-planet Keplerian fit, (v) a first-order, evolving two-planet Keplerian fit, (vi) and a first-order, evolving two-planet fit where the long-period companion is modeled as a quadratic trend.

In case (i), the model can be described by 13 free parameters, five of which describe the orbit—period (P), planet mass (M_p), time of periastron passage (t_p), eccentricity (e) and argument of periastron (ω), which are parameterized as $\sqrt{e} \sin \omega$ and $\sqrt{e} \cos \omega$ —two of which describe a linear ($\dot{\gamma}$) and quadratic ($\ddot{\gamma}$) trend with time,¹¹ and six which correspond to the offsets (γ) and RV jitter terms for each of the RV data sets. RV jitter describes the instrumental and astrophysical stochastic signals in the data. Astrophysical signals originate from stellar variability such as inhomogeneities on the stellar surface, pressure-mode oscillations, and granulation. Since each instrument has its own noise characteristics, it is common to fit for a jitter term for each instrument. We note that RV models are commonly parametrized using semi-amplitude (K) rather than mass. However, when e and ω are allowed to vary over time for an evolving planet model, this parameterization allows mass to vary over time, which is unphysical. Parameterizing the RV model in terms of mass prevents this and instead only allows K to vary as a function of e and ω . In case (ii), we gain an additional five orbital parameters for a secondary companion, which sums to 18 free parameters.¹² In case (iii), the secondary companion is modeled as a second-order background trend so this adds a linear and quadratic term and thereby two additional free parameters. In case (iv), we add first-order polynomials for e and/or ω and this adds one free parameter per polynomial. In case (v), we add an additional five parameters to fit for the orbital parameters of a secondary companion. Lastly, in case (vi), we instead model the secondary companion as a linear and quadratic trend so this adds two free parameters.

Once a given orbital configuration is chosen, we sample our parameter space using `edmcmc` (Vanderburg 2021),¹³ which is an implementation of Markov Chain Monte Carlo (MCMC) that incorporates differential evolution (DE; Ter Braak 2006). DE is a genetic algorithm that solves the problem of choosing an

¹⁰ We note that we accounted for the way that `radvel` used ω_p rather than ω_* in its implementation (Householder & Weiss 2022) and we only report throughout this paper.

¹¹ In the case of HAT-P-2, we have a long-period secondary companion that has a period close to the baseline. For this reason, we do not include the linear and quadratic background trends to prevent degeneracies. Thus, we only have 11 free parameters for model (i) rather than 13.

¹² We again do not include the linear and quadratic trends for HAT-P-2 so we have 16 free parameters.

¹³ <https://github.com/avanderburg/edmcmc>

⁹ <http://archives.ia2.inaf.it/tng/>

appropriate scale and orientation for the jumping distribution, which significantly speeds up the fitting process.

After performing the fit, the pipeline produces several diagnostic plots and performance metrics (described in Section 3.2) to assess goodness of fit. Convergence of the parameters is determined using the Gelman–Rubin statistic (Gelman & Rubin 1992), where our Gelman–Rubin threshold is <1.02 . We computed 10,000 MCMC chains and discarded the first 25% burn-in samples to produce our posterior samples. We implemented Gaussian priors to the P and t_p parameters based on transit and occultation times from previous studies (Ivshina & Winn 2022). For our models that include a Keplerian long-period companion, we also apply Gaussian priors to the companion’s period (P_2) and time of periastron passage (t_{p2}) based on the astrometry analysis described in Section 3.3 since the RVs do not sufficiently span its orbital period to constrain these parameters alone. To derive our final parameter values, we computed the median and 68.3% confidence intervals. The results for our comparison of models (i)–(vi) are described in Section 4.

3.2. Performance Metrics

We use four different metrics to assess the goodness of fit of our various orbital models: (i) the loglikelihood, (ii) the reduced chi-squared statistic (χ_r^2), (iii) the Bayesian information criterion (BIC; Schwarz 1978), (iv) and the Akaike information criterion (AIC; Akaike 1974). Each of these metrics have different advantages and emphasize different features of the fitted models. Generally, each metric penalizes the number of free parameters in a different way, and the AIC tends to be the least punitive of more complex models. In our analysis, these different metrics all provide consistent results. Each metric is described in additional detail in the Appendix.

3.3. Joint Fit of Astrometry and Radial Velocities

In order to further investigate the possibility of a long-period companion to HAT-P-2 b, we performed a joint fit of the RV and astrometric data sets. The model used to perform this joint analysis is described in detail in Venner et al. (2021). In summary, we jointly fit the two data sets with a three-body Keplerian model with 22 variable parameters: the stellar mass and parallax, which were assigned Gaussian priors of $1.33 \pm 0.03 M_\odot$ and 7.781 ± 0.012 mas respectively; P , K , e , ω , t_p for both companions; orbital inclination (i) and longitude of the ascending node (Ω) for the outer companion; proper motion of system barycentre parameters ($\mu_{\text{bary,RA}}$, $\mu_{\text{bary,Dec}}$); and normalization and jitter parameters for each RV data set. In comparison to the models described in Section 3.1, this is equivalent to a stable two-planet Keplerian fit.

Cursory examination of the model reveals a degeneracy between P and e for the outer companion, arising due to incomplete coverage of the orbit. If the outer planet has a shorter orbital period, it is more likely to be observed during its periastron passage than for longer orbital periods. We account for this in the same way as Blunt et al. (2019) and Venner et al. (2022) by adopting an informed prior on the orbital period such that

$$\mathcal{P}(P, t_d, B) = \begin{cases} 1 & \text{if } (P - t_d) < B \\ (B + t_d)/P & \text{otherwise} \end{cases}, \quad (1)$$

where \mathcal{P} is the probability of observing periastron passage, P is the orbital period, t_d is the duration of periastron passage, and B is the baseline of observations. This prior is analogous to the

period priors used for long-period transiting exoplanets (e.g., Vanderburg et al. 2016; Kipping 2018). Imposing this prior slightly penalizes orbital solutions where the periastron passage of a long orbit happens to occur during the comparatively short span of observations. This discourages our model from fine-tuned long-period orbital solutions for the outer companion, without excluding them entirely. Blunt et al. (2019) tested a range of values for t_d and found that their orbital fits were indistinguishable, and thus chose $t_d = 0$. We do the same in this analysis.

We again use `edmc` (Vanderburg 2021) to explore the parameter space of the model. We produce posterior samples by discarding the first 25% of the chain as burn-in and save every hundredth step for each walker. We extract the median and 68.3% confidence intervals for the parameters from the samples and compute the same confidence intervals for physical parameters that can be derived (i.e., companion mass).

4. Results

4.1. Comparing Radial Velocity Orbital Fits

For each of our four models we computed the performance metrics described in Section 3.2, and list them in Tables 1 and 2. First, we can compare the stable one-planet model with the stable model that allows for a long-period companion modeled as either a Keplerian or a quadratic trend. We find that the stable two-planet model (two Keplerians) has a significantly lower reduced $\chi_r^2 = 1.035$, lower $\Delta\text{BIC} = 14.90$, lower $\Delta\text{AIC} = 12.26$, and higher loglikelihood = -432.05 compared to the one-planet model ($\chi_r^2 = 2.806$, $\Delta\text{BIC} = 165.18$, $\Delta\text{AIC} = 175.72$, loglikelihood = -518.7). Furthermore, the stable two-planet model (Keplerian + quadratic) has a similar reduced $\chi_r^2 = 1.045$, similar $\Delta\text{BIC} = 21.16$, $\Delta\text{AIC} = 15.90$, and similar loglikelihood = -432.87 compared to the other two-planet model. To visually examine these orbital models, we plot the median fit along with 100 random draws for all three of these models in Figures 1(a)–(f). Overall, the two planet models (either the two Keplerian or Keplerian + quadratic version) are favored in the comparison of these stable orbit models.

Next, we can compare various evolving orbit scenarios for HAT-P-2 b. We include the one-planet (Keplerian), two-planet (two Keplerians), and two-planet (Keplerian + quadratic) scenarios, where HAT-P-2 b’s e and ω can vary linearly with time. We find that the evolving one-planet model ($\chi_r^2 = 2.504$, $\Delta\text{BIC} = 142.47$, $\Delta\text{AIC} = 147.74$, loglikelihood = -502.788) provides a marginally better fit to the observations than a stable one-planet model. This is not a significant difference, however. The evolving one-planet model is plotted in Figures 2(a), (b). Next, we find that model (v), the evolving two-planet (two Keplerians) model, provides a slightly better fit ($\chi_r^2 = 0.963$, $\Delta\text{BIC} = 10.181$, $\Delta\text{AIC} = 7.546$, loglikelihood = -429.691) than model (ii), the stable two-planet (two Keplerians) model. Overall, we find that model (vi), the evolving two-planet model (Keplerian + quadratic) provides the best fit with the lowest $\chi_r^2 = 0.891$, the lowest BIC = 909.453, the lowest AIC = 877.836, and the highest loglikelihood = -426.918 . We plot this model in Figures 2(e), (f). We note that we also performed some additional tests to see how the rate of evolution for e and ω and their significance are impacted by how the long-term

Table 1
Converged MCMC Results for Each of the Stable Orbital Models and their Goodness-of-fit Values

Model	(i) Stable One Planet (Keplerian)	(ii) Stable Two Planets (Two Keplerians)	(iii) Stable Two Planets (Keplerian + Quadratic)
Goodness-of-fit metrics:			
Reduced χ_r^2	2.806	1.035	1.045
Loglikelihood	-518.77	-432.05	-432.87
ΔBIC^a	165.18	14.90	21.16
ΔAIC^a	175.72	12.26	15.90
MCMC values:			
M_p (M_j)	$9.233^{+0.099}_{-0.098}$	$9.033^{+0.010}_{-0.099}$	$8.998^{+0.010}_{-0.098}$
P (days)	$5.63346961^{+0.00000064}_{-0.00000064}$	$5.63346961^{+0.00000064}_{-0.00000064}$	$5.63346960^{+0.00000064}_{-0.00000064}$
$T_p-2455000$ (days)	$289.46980^{+0.00034}_{-0.00034}$	$289.48642^{+0.00033}_{-0.00033}$	$289.48642^{+0.00034}_{-0.00034}$
e_0	$0.4990^{+0.0085}_{-0.0086}$	$0.5003^{+0.0090}_{-0.0089}$	$0.4960^{+0.0088}_{-0.0088}$
ω_0 ($^\circ$)	$188.25^{+0.39}_{-0.39}$	$189.62^{+0.40}_{-0.40}$	$189.49^{+0.41}_{-0.41}$
$\gamma_{\text{HARPS-2013-2015}}$	$-26.8^{+8.5}_{-8.6}$	51^{+19}_{-17}	150^{+16}_{-16}
$\gamma_{\text{HARPS-2015-2017}}$	-20.8^{+18}_{-18}	35^{+24}_{-23}	136^{+22}_{-22}
γ_{HIRES}	$-33.8^{+4.9}_{-4.9}$	-170^{+17}_{-14}	$77.4^{+9.9}_{-9.8}$
Linear ($\dot{\gamma}$)			$-0.117_{-0.011} + 0.011$
Quadratic ($\ddot{\gamma}$)			$0.0000194^{+0.0000023}_{-0.0000023}$
M_{p2} (M_j)		$12.1^{+2.9}_{-2.2}$	
P_2 (days)		8721^{+1407}_{-1141}	
$T_{p2}-2455000$ (days)		-9092^{+287}_{-400}	
e_{02}		$0.313^{+0.080}_{-0.069}$	
ω_{02} ($^\circ$)		44^{+17}_{-18}	

Notes. For each of the models, we specify whether the planets were modeled as a Keplerian or a quadratic trend.

^a The ΔBIC and ΔAIC are computed by subtracting the BIC and AIC, respectively, corresponding to model (iv) two Planets (Keplerian + Quadratic), from the BIC and AIC values. The results for model (iv) are listed in Table 2.

companion is modeled, and we include this in the discussion (Section 5.1.4).

4.2. Astrometric-Radial Velocity Joint Fit

The results of the previous section strongly suggest the presence of an outer companion in the system, as has been found by past authors (Lewis et al. 2013; Knutson et al. 2014; Bonomo et al. 2017; Ment et al. 2018). Furthermore, our 5 yr extension of the HIRES time series allows us to clearly observe nonlinearity in the RV acceleration. Previously, Knutson et al. (2014) constrained the mass of the outer companion to 8–200 M_j and the semimajor axis to 4–31 au based on the nondetection of a stellar companion in direct imaging. The strong orbital motion suggests that the companion has a relatively short period, and hence a mass on the lower end of this range.

HAT-P-2 has been observed by both Hipparcos and Gaia, allowing us to make use of Hipparcos-Gaia astrometry (Brandt 2018, 2021) to place additional constraints on the outer companion. We expect that even the lowest-mass solutions should produce a detectable ($\gtrsim 0.2 \text{ mas yr}^{-1}$) astrometric signal based on the RV signal, but surprisingly we find that the Hipparcos-Gaia astrometry of HAT-P-2 is consistent with zero net acceleration. A possible explanation for this is that the orbital period is close to the 25 yr astrometric timespan. Specifically, if the orbital inclination is close to edge-on and the outer companion is at conjunction during both the Hipparcos and Gaia observations, then there will be no net acceleration between the Gaia proper motion and Hipparcos-Gaia mean proper motion, as observed.

This is borne out by our joint fit to the RVs and astrometry, the results of which we plot in Figure 3. As anticipated, we find an orbital period of the outer companion of $23.2^{+7.1}_{-4.1}$ yr, comparable to a 25 yr timespan of the astrometric data. To demonstrate the importance of the astrometry for this result, in Figure 4 we compare the period distribution from our joint fit with that of an RV-only model. The astrometric nondetection allows us to exclude orbital periods significantly longer than 15,000 days at 95% confidence. Furthermore, the nondetection constrains the orbital inclination to $\approx 90^\circ$ as this is the only orbital configuration consistent with zero net astrometric acceleration over the span of observations.

The key posterior parameters of the outer companion are as follows:

$$\begin{aligned}
 P_c &= 8500^{+2600}_{-1500} \text{ days} \\
 K_c &= 89^{+39}_{-13} \text{ m s}^{-1} \\
 e_c &= 0.37^{+0.13}_{-0.12} \\
 \omega_c &= 38^\circ \pm 32^\circ \\
 T_{p,c} &= 2454150^{+430}_{-800} \text{ BJD} \\
 i_c &= 90^\circ \pm 16^\circ.
 \end{aligned} \tag{2}$$

The longitude of the ascending node (Ω) is unconstrained. With the orbital period and inclination resolved, we find that the mass of this second companion is $10.7^{+5.2}_{-2.2} M_j$. The mass posterior is entirely substellar and corresponds to a substellar-mass object, comparable in mass to HAT-P-2 b, which straddles the deuterium-burning limit at 13 M_j . We hence

Table 2
Converged MCMC Results for Each of the Evolving Orbital Models and their Goodness-of-fit Values

Model	(iv) Evolving One Planet (Keplerian)	(v) Evolving Two Planets (Two Keplerians)	(vi) Evolving Two Planets (Keplerian + Quadratic)
Goodness-of-fit metrics:			
Reduced χ_r^2	2.504	0.963	0.891
Loglikelihood	-502.788	-429.691	-426.918
ΔBIC^b	142.47	10.181	0.00
ΔAIC^b	147.74	7.546	0.00
MCMC values:			
M_p (M_J)	$9.27^{+0.10}_{-0.10}$	$9.02^{+0.10}_{-0.10}$	$9.04^{+0.10}_{-0.10}$
P (days)	$5.63365^{+0.000039}_{-0.000040}$	$5.63346964^{+0.00000063}_{-0.00000062}$	$5.633587^{+0.000044}_{-0.000043}$
T_p (days)	$289.440^{+0.011}_{-0.012}$	$289.48643^{+0.00033}_{-0.00034}$	$289.48642^{+0.00034}_{-0.00034}$
$e0$	$0.499^{+0.010}_{-0.011}$	$0.502^{+0.011}_{-0.012}$	$0.495^{+0.011}_{-0.011}$
de/dt^a (1 yr $^{-1}$)	$1.75^{+1.71}_{-1.68} \times 10^{-3}$	$-7.3^{+19.0}_{-18.0} \times 10^{-4}$	$7.7^{+18.6}_{-18.6} \times 10^{-4}$
$\omega0$ ($^\circ$)	$184.6^{+1.1}_{-1.1}$	$188.80^{+0.57}_{-0.58}$	$185.9^{+1.2}_{-1.2}$
$d\omega/dt^a$ ($^\circ$ yr $^{-1}$)	$1.12^{+0.22}_{-0.22}$	$0.228^{+0.11}_{-0.11}$	$0.76^{+0.24}_{-0.24}$
$\gamma_{\text{HARPS-2013-2015}}$	$-23.1^{+8.5}_{-8.7}$	45^{+18}_{-16}	142^{+16}_{-16}
$\gamma_{\text{HARPS-2015-2017}}$	-24^{+19}_{-19}	41.9^{+23}_{-22}	134^{+23}_{-23}
γ_{HIRES}	$-35.9^{+5.0}_{-5.0}$	-20.8^{+15}_{-13}	71^{+10}_{-10}
Linear ($\dot{\gamma}$)			$-0.110^{+0.011}_{-0.011}$
Quadratic ($\ddot{\gamma}$)			$1.78^{+0.24}_{-0.25} \times 10^{-5}$
M_{p2} (M_J)		$11.6^{+2.8}_{-2.0}$	
$P2$ (days)		8777^{+1400}_{-1200}	
$Tp2$ (days)		-900^{+300}_{-380}	
$e02$		$0.346^{+0.078}_{-0.072}$	
$\omega02$ ($^\circ$)		$43.0^{+16.0}_{-19.5}$	

Notes. For each of the models, we specify whether the planets were modeled as a Keplerian or a quadratic trend.

^a Only the orbital parameters of HAT-P-2 b are allowed to vary over time.

^b The ΔBIC and ΔAIC are computed by subtracting the BIC and AIC, respectively, corresponding to model (iv) Two Planets (Keplerian + Quadratic), from the BIC and AIC values.

designate this companion as HAT-P-2 c, confirming the presence of a second substellar-mass companion in the HAT-P-2 system. We note that the parameters of HAT-P-2 c derived from this joint astrometric-RV fit agree within error with the RV fits in Tables 1 and 2. The parameter values for HAT-P-2 c from the joint fit should be considered more robust.

5. Discussion

5.1. Orbital Evolution of HAT-P-2 b

5.1.1. Rates of Orbital Evolution

From our orbital fitting analyses, we find that although a two-planet,¹⁴ evolving orbit model that allows e and ω to vary linearly with time fits the RV measurements best, the orbital parameters of HAT-P-2 c are poorly constrained in these RV models and follow-up observations are required to fully confirm or rule out orbital evolution in HAT-P-2 b. For this model, we find that $d\omega/dt = 0.76^{+0.24}_{-0.24}$ yr $^{-1}$ and $de/dt = 7.67^{+13.2}_{-18.5} \times 10^{-4}$ yr $^{-1}$, which correspond to 3.23σ and 0.4σ detections, respectively. In Figure 5, we illustrate how these changes in ω and e correspond to changes in the shape of the orbit over time. Although these rates of change agree within error with the rates ($d\omega/dt = 0.91^\circ \pm 0.31^\circ$ yr $^{-1}$, $de/dt = 8.9 \pm 2.8 \times 10^{-4}$ yr $^{-1}$) found in de Wit et al. (2017), they

found a slightly more significant change in e . Additional RV measurements in the next few years should allow for a further refinement of de/dt and $d\omega/dt$ as described in Section 5.1.6. Specific choices in how HAT-P-2 c's long-term signal was modeled may also offer an explanation for the slight differences in evolution rates found in these different analyses, as described in detail in Sections 5.1.2 and 5.1.4.

5.1.2. Comparison to Radial Velocity Analysis in de Wit et al. (2017)

In de Wit et al. (2017), the long-term trend corresponding the outer companion and the orbital evolution were modeled differently than in this analysis. In particular, the data available to de Wit et al. (2017) only sampled the linearly decreasing component of the long-term trend, and therefore the authors modeled the outer companion as a linear trend rather than a quadratic or Keplerian. Now, with an additional 5 yr of RV data, we were able to model the outer companion as a quadratic or Keplerian instead. For completeness, we also included a test wherein we approximated the outer companion as a linear trend, as described in Section 5.1.4.

In addition to modeling the outer companion more accurately in our analysis, we also were able to model the orbital evolution in a more robust way with the availability of more RVs. de Wit et al. (2017) checked for changes in e and ω by (i) splitting the RV data into two approximately equal halves (data prior and after BJD 2454604), and (ii) fitting each data set independently for an average value of e and ω . de Wit et al. (2017) then computed an estimate for the trends in e and ω based on the difference in values

¹⁴ Where HAT-P-2 b is modeled as a Keplerian and HAT-P-2 c is modeled as a quadratic trend.

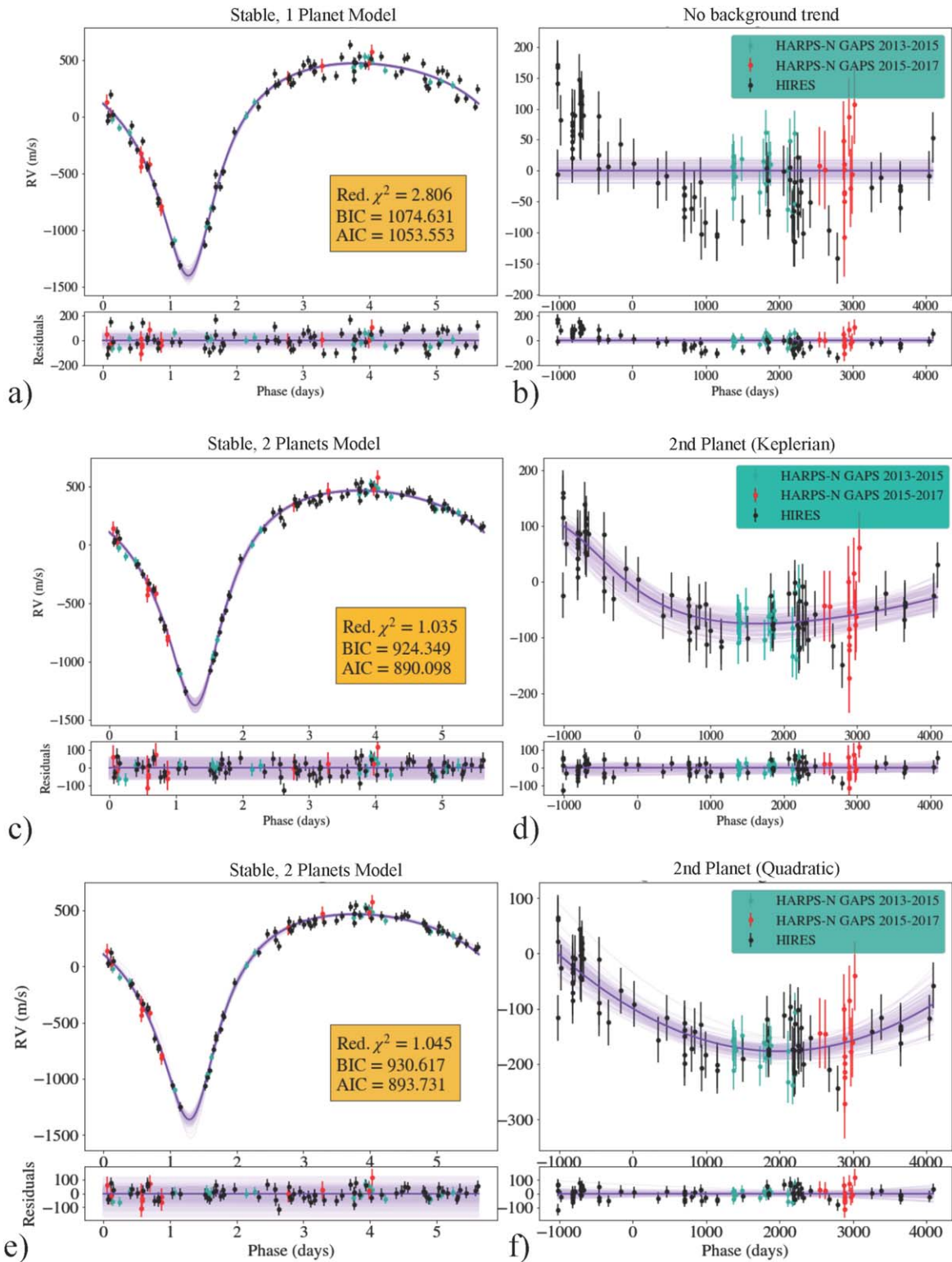


Figure 1. Comparison of our stable, nonevolving orbital models. From top to bottom, we include the stable one-planet model with no background trends (a), (b); the stable two-planet model with the long-period companion modeled as a Keplerian (c), (d); and the stable two-planet model with the long-period companion modeled as a quadratic trend (e), (f). For more details on these orbital models, see Section 3.1. In each of the left-hand panels (a), (c), (e), we plot the orbital fit of HAT-P-2 b minus a secondary companion (or no companion if this was not included in the model). The data is color-coded by instrument (turquoise = HARPS-N 2013-2015, red = HARPS-N 2015-2017, black = HIRES). The median model is plotted in dark purple and 100 draws from the posteriors are plotted in light purple. In each of the right-hand panels (b), (d), (f), we plot the secondary companion (or no trend/companion if this was not included in the model) minus the median HAT-P-2 b model. We also include the goodness-of-fit metrics corresponding to each orbital model in the yellow box. “Red. χ_r^2 ” is an abbreviation for reduced χ_r^2 .

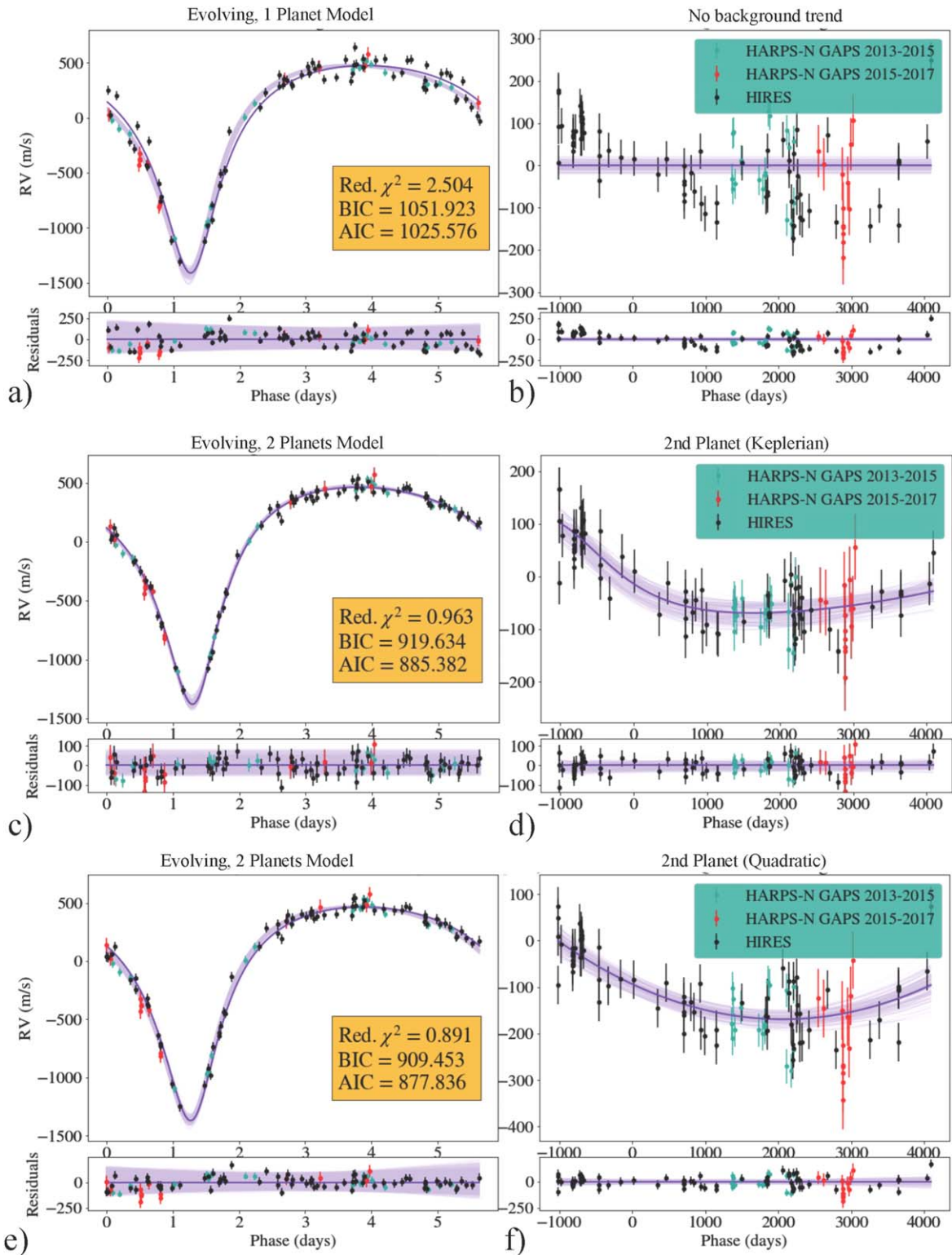


Figure 2. Comparison of our evolving orbital models. From top to bottom, we include the evolving one-planet model with no background trends (a), (b); the evolving two-planet model with the long-period companion modeled as a Keplerian (c), (d); and the evolving two-planet model with the long-period companion modeled as a quadratic trend (e), (f). For more details on these orbital models, see Section 3.1. The color-coding is identical to Figure 1.

for each of these halves of the data. In this analysis, we instead fit the entire RV data set simultaneously and define $e = de/dt \cdot \text{time} + e_0$, $\omega = d\omega/dt \cdot \text{time} + \omega_0$ such that we fit for

de/dt and $d\omega/dt$ directly. This approach should require that the trend is more persistent across the entire RV baseline and provide more robust estimates of the uncertainties on the trends as well.

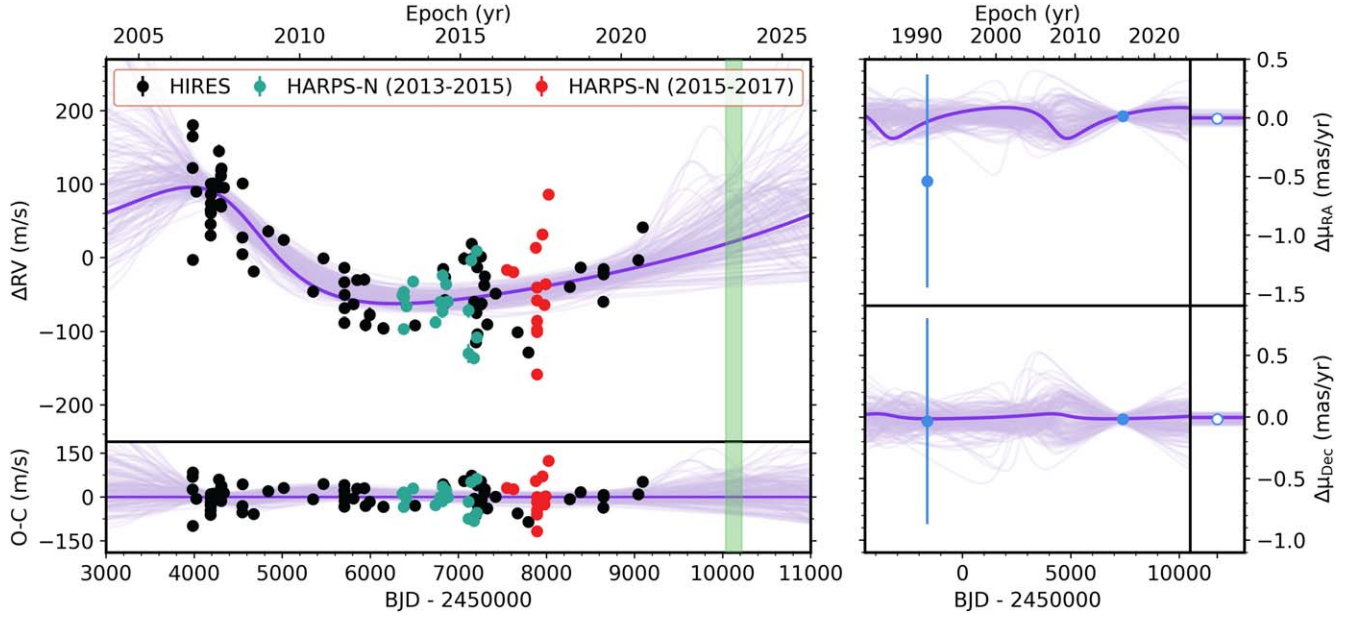


Figure 3. The orbit of HAT-P-2 c from a joint fit to the RVs (left) and astrometry (right). Colors are as in Figure 1. The astrometry is consistent with zero net acceleration; the limits of this nondetection allow us to place useful constraints on the orbital period and inclination ($P_c = 8500_{-1500}^{+2600}$ days, $i_c = 90^\circ \pm 16^\circ$). The resulting mass of HAT-P-2 c is $10.7_{-2.2}^{+3.2} M_J$, establishing it as a substellar-mass object. We indicate the next observing window (2023 April 1–2023 September 28) with green shading. Further RV observations would help to improve constraints on the companion’s orbit.

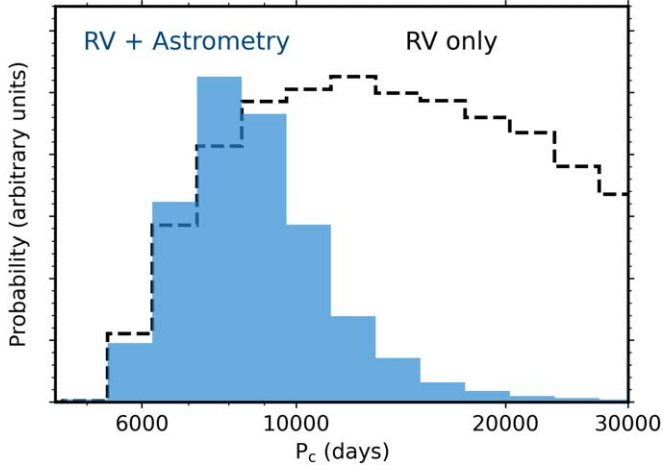


Figure 4. The orbital period distribution of HAT-P-2 c for our joint RV-astrometry fit (blue) vs. RV-only (black).

5.1.3. Can the Change in ω Be Explained by General Relativity Alone?

We computed the rate of change expected from general relativity (GR), where

$$\hat{\omega}_{\text{GR}} = \frac{3GM_*}{ac^2(1-e^2)}n, \quad (3)$$

$$= 1.185 \cdot 10^{-2} \text{ degrees yr}^{-1}, \quad (4)$$

where n is the Keplerian mean motion, a is the semimajor axis, and M_* is the mass of the star. We find that for HAT-P-2 b, $\hat{\omega}_{\text{GR}} = 1.185 \cdot 10^{-2} \text{ degrees yr}^{-1}$. However, in our best-fit model, we find $\hat{\omega} = 0^\circ.76 \pm 0^\circ.24 \text{ yr}^{-1}$, which is nearly 65 times the rate of change expected from GR. Thus, this type of rate of change cannot be explained by GR alone. Tidal planet–

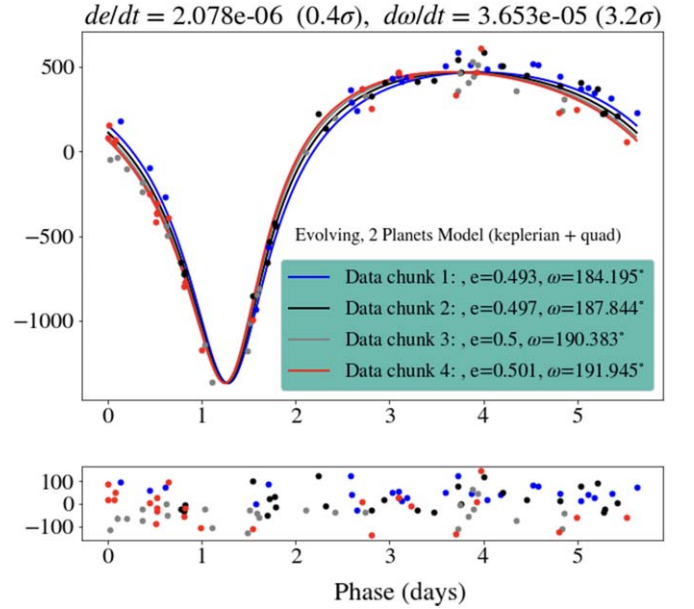


Figure 5. Variation in orbital shape over time for HAT-P-2 as e and ω increase linearly over time. The long-period companion is modeled as a quadratic trend here. The trends in e and ω were fit using the entire data set, but for visualization the data is split into four equal-sized chunks (~ 25 observations per chunk) here. The median model corresponding to that time period is computed using the median e and ω for the corresponding time period.

star interactions may potentially be able to explain this type of rapid change.

5.1.4. The Impact of Modeling Choices for Planet c on the Rate of Evolution of e and ω

Since previous analyses (Bonomo et al. 2017; de Wit et al. 2017) modeled the long-period companion as linear or quadratic trends, we performed additional tests wherein we

Table 3

Comparison of Evolving Orbit Models Where the Second Companion Is Not Modeled or Modeled as a Linear Trend, a Quadratic Trend, or a Keplerian

Model for HAT-P-2 c	None	Linear	Quadratic	Keplerian
χ_r^2	2.503	1.440	0.891	0.963
ΔBIC^a	142.47	46.77	0.00	10.181
ΔAIC^a	147.74	49.405	0.00	7.5460363
de/dt (1 yr ⁻¹)	$1.75^{+1.71}_{-1.68} \times 10^{-3}$	$3.28^{+1.72}_{-1.75} \times 10^{-3}$	$7.7^{+18.6}_{-18.6} \times 10^{-4}$	$-7.3^{+19.0}_{-18.0} \times 10^{-4}$
$d\omega/dt$ (° yr ⁻¹)	$1.12^{+0.22}_{-0.22}$	$1.12^{+0.22}_{-0.22}$	$0.76^{+0.24}_{-0.24}$	$0.228^{+0.11}_{-0.11}$
$\sigma_{de/dt}$	1.03	1.90	0.41	0.32
$\sigma_{d\omega/dt}$	5.20	5.11	3.23	2.11

Note.

^a The ΔBIC and ΔAIC are computed by subtracting the BIC and AIC, respectively, corresponding to model (iv) Two Planets (Keplerian + Quadratic) from the BIC and AIC values. Within this table, that is equivalent to subtracting the ‘‘Quadratic’’ model BIC and AIC values.

modeled the second companion in the same way and investigated its impact on the derived rate of orbital evolution. In Table 3, we list the derived rates of orbital evolution and their significance of detection when not modeling the outer companion and when modeling the outer companion as a linear trend, a quadratic trend, or as a Keplerian. We find that when we do not model HAT-P-2 c, the significance of the trend in ω (5.2σ) is highest and the significance of the trend in e (1.03σ) is second highest among these models. The derived rates of evolution are also among the highest among these models ($de/dt = 1.75^{+1.71}_{-1.68} \times 10^{-3} \text{ yr}^{-1}$, $d\omega/dt = 1.12^{+0.22}_{-0.22} \text{ yr}^{-1}$). When we model HAT-p-2 c as a linear trend, the significance of the trend in e (1.9σ) increases and the significance of $d\omega/dt$ is marginally lower but still a 5.1σ trend. The rates are the highest with $de/dt = 3.28^{+1.72}_{-1.75} \times 10^{-3} \text{ yr}^{-1}$ and $d\omega/dt = 1.12^{+0.22}_{-0.22} \text{ yr}^{-1}$.

For the quadratic model, the significance of both trends decreases ($\sigma_{de/dt} = 0.41$, $\sigma_{d\omega/dt} = 3.23$) and the rates also decrease ($de/dt = 7.7^{+18.6}_{-18.6} \times 10^{-4} \text{ yr}^{-1}$, $d\omega/dt = 0.76^{+0.24}_{-0.24} \text{ yr}^{-1}$). For the Keplerian model, we find that significance in de/dt slightly increases ($\sigma_{de/dt} = 0.32$) and the significance in $d\omega/dt$ also decreases ($\sigma_{d\omega/dt} = 2.11$). The rate of evolution continues to decrease for $d\omega/dt$ ($d\omega/dt = 0.228^{+0.11}_{-0.11} \text{ yr}^{-1}$) and the direction of de/dt changes ($de/dt = -7.3^{+19.0}_{-18.0} \times 10^{-4} \text{ yr}^{-1}$). However, this trend in e is so insignificant, indicating that this parameter is unconstrained by the data, and so we do not attribute a physical interpretation to this change in sign. Clearly, the exact modeling choices of HAT-P-2 c strongly affect the rates and significance of the evolution rates derived for HAT-P-2 b. The Keplerian model is the most physically motivated, but the period is still relatively unconstrained ($P_c = 8500^{+2600}_{-1500}$ days), and so are many of the other orbital parameters. Thus, further monitoring of the HAT-P-2 system to allow us to model the long-term RV changes induced by HAT-P-2 c most accurately are necessary and should allow us to constrain the rates and possible evolution of HAT-P-2 b as well. In particular, we propose follow-up RVs to constrain the orbital parameters of HAT-P-2 c and follow-up transit and eclipse observations to solve precisely for the current values of e and ω , which when combined with archival Spitzer data should allow us to definitively constrain the rate of evolution.

5.1.5. Spitzer Transits and Secondary Eclipses

To get additional constraints on e and ω and look for trends, we reprocessed and analyzed $4.5 \mu\text{m}$ Spitzer transit and secondary-eclipse measurements using the pipeline described in Berardo et al. (2019). We computed the best-fit systematic model using the pixel-

level decorrelation technique (Deming et al. 2015). We analyzed the primary and secondary eclipses by splitting the data into three chunks (2011, 2013, and 2015 observations) and performed three independent fits to obtain a measurements of e and ω for each time period and look for changes in their values. For the 2011 observations, we find $e = 0.5104 \pm 0.0025$ and $\omega = 189.10^\circ \pm 2.19^\circ$. For 2015 observations, we find $e = 0.5128 \pm 0.0014$ and $\omega = 190.95^\circ \pm 1.23^\circ$. Since the 2013 observations only included eclipses and no transits, we did not have the transit eclipse pair that is necessary to constrain e for the 2013 window. Overall the Spitzer transit and eclipse measurements provide some constraints on the possible rates of change for e and ω , but they only contain three to four transits/eclipses in each subset. With this little amount of data available for each of these subsets, we do not get enough precision to accurately measure drifts in e . We plan to propose for JWST observations such that we can get the necessary precision to further constrain the rates of change of e and ω .

5.1.6. Radial Velocity Sensitivity Analysis

In order to further characterize the HAT-P-2 system such that we can increase the significance of detection of the orbital evolution (or lack thereof), we performed a sensitivity analysis for the next observing window. In Figure 6, we plot the expected RVs for the first orbit of the spring–fall 2023 observing season (2023 April 1–2023 April 5). The expected RVs for a stable orbit will diverge significantly from an evolving orbit model and we should be able to clearly distinguish the two scenarios as seen in Figures 6(b), (c). In Figure A1, we plot the entire next observing window, which illustrates that we should also be able to distinguish clearly between the one- or two-planet models and further constrain the period of a potential HAT-P-2 c. Thus, constraining the period of the long-period companion would require three to four RV measurements on HIRES/Keck I. This could be done anytime in the observing window (2023 April 1–2023 September 28) and would extend the RV baseline from 14 to 17 yr. However, also detecting the orbital evolution would require additional RVs and would place constraints on the timing of the observations. In particular, to get a 6σ detection of the orbital evolution, we require nine total RV measurements spanning three orbital periods (i.e., three RVs per orbit). The particular orbital phases are indicated in green in Figures 6(b), (c). Although taking the RV observations at these orbital phases would be required, the observations could be taken for any orbit during the observing window.

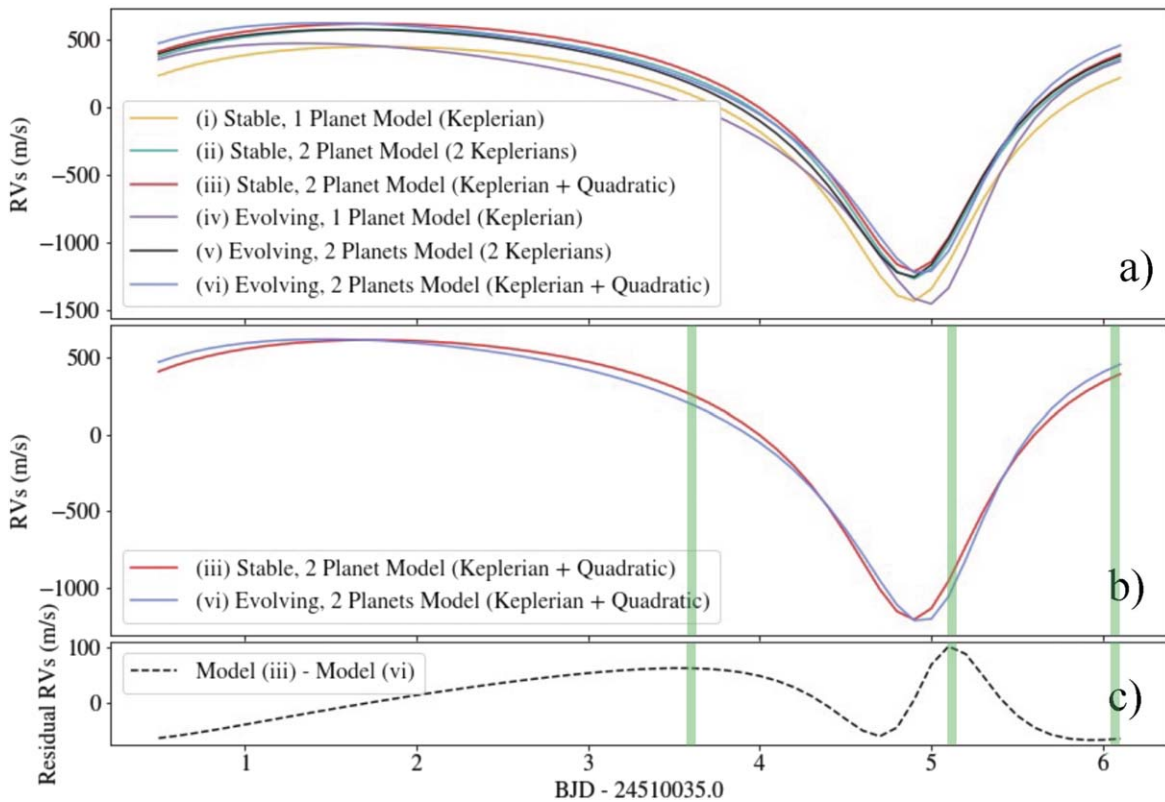


Figure 6. Expected RVs for the first orbit of the current observing window (2023 April 1–2023 April 5). (a) This is a zoomed-in version of Figure A1 and demonstrates the differences in expected RVs more clearly for a singular orbit. (b) The two best-fit models (ii), (vi) are plotted side by side to compare their differences. In green, we indicate the three orbital phases we propose to sample three times to detect the orbital evolution or lack thereof. (c) The residual RVs from subtracting the expected RVs from model (vi) from model (iii).

5.2. HAT-P-2 c

The presence of a long-period outer companion to HAT-P-2 has been suggested in previous studies on the basis of a significant RV acceleration (Lewis et al. 2013; Knutson et al. 2014; Bonomo et al. 2017; Ment et al. 2018). We have constrained the orbit of this companion for the first time by jointly fitting the RVs with astrometry from the Hipparcos-Gaia Catalog of Accelerations (Brandt 2018, 2021). Though no acceleration is detected in the Hipparcos-Gaia astrometry, this nondetection is sufficiently informative to constrain the orbit of the second companion. HAT-P-2 c is a $10.7^{+5.2}_{-2.2} M_j$ substellar-mass object with an orbital period of $P_c = 8500^{+2600}_{-1500}$ days, placing it among the longest-period substellar companions that have ever been discovered from RVs.

The constraints of the astrometric nondetection require HAT-P-2 c to have an edge-on orbital inclination ($i_c = 90^\circ \pm 16^\circ$), as any other configuration would produce a detectable astrometric signal. This is comparable to the result of Errico et al. (2022), who determined the true mass of the long-period planet HD 83443 c from an astrometric nondetection. HAT-P-2 c’s orbital inclination is consistent with HAT-P-2 b, which in turn has a low projected obliquity from the host star’s rotational axis (Winn et al. 2007; Albrecht et al. 2012). This suggests that the orbital and rotational planes in the HAT-P-2 system are compatible with alignment, agreeing well with the conclusions of Becker et al. (2017), who found that outer planets in Hot Jupiter systems must generally have low mutual inclinations to reproduce the low obliquities observed in these systems. The absence of strong misalignments in the HAT-P-2 system appears inconsistent with a chaotic dynamical

history, which may be surprising considering the remarkably high orbital eccentricity of HAT-P-2 b. The formation history of this unusual planetary system will be an interesting topic to explore in future studies.

6. Future Work

We have proposed for RV follow-up observations to further constrain the period and orbital parameters of HAT-P-2 c, which will help us determine the magnitude and significance of orbital evolution for HAT-P-2 b (or lack thereof). In particular, we proposed to observe during specific phases of the orbit which have the information content necessary to disentangle between the one- to two-planet and evolving or nonevolving scenarios, as further described in Section 5.1.6.

In addition, we plan to propose for a JWST partial phase curves of the system with three goals in mind:

1. To obtain ultra-precise transit and eclipse timing measurements: These measurements will enable us to get extremely tight constraints on the current values of e and ω , and thereby constrain their evolution.
2. To measure the transient heating of HAT-P-2 b: Due to its high-eccentricity and short-period orbit, HAT-P-2 b is an ideal target for studying how atmospheres redistribute the time-varying heat flux from host stars. Analogous to Lewis et al. (2014), we would propose to measure the transient heating and use 3D atmospheric circulation models to further our understanding of the atmospheric response of exoplanets on highly eccentric orbits.

- To follow-up on the planet-induced oscillations observed on the star noted in de Wit et al. (2017) and check for wavelength-dependence of these oscillations: This will also allow us to construct a 2D heat map of HAT-P-2 b's surface, which was not possible in previous papers due to the complications added by the oscillations.

7. Conclusion

We developed a modular orbital evolution fitting pipeline that allowed us to perform apples-to-apples comparison between various dynamical scenarios that may explain observed RV variation in the HAT-P-2 system. Using this pipeline, we confirmed that the hints of rapid change in argument of periastron (ω) and eccentricity (e) noted in de Wit et al. (2017) appear to persist with an additional 5 yr of RV data. However, the significance and exact rates of this evolution is highly dependent on the modeling of the long-period companion and requires additional follow-up observations to constrain. The largest changes in ω are significantly larger than what would be expected solely from general relativistic precession and could instead be explained by tidal planet–star interactions. Since these precession rates are not possible to explain with GR alone, further investigation to model the tidal planet–star interactions with stellar evolution and pulsation codes (MESA; Paxton et al. 2011; GYRE; Townsend et al. 2014) is warranted. We also ran a joint fit with Hipparcos-Gaia astrometry and the RV measurements. This joint fit allowed us to put precise constraints on the outer companion in the system, HAT-P-2 c, which we find to be substellar. Furthermore, this work sets the stage for applying our orbital evolution fitting pipeline to a larger sample of stars that host eccentric Hot Jupiters, with the ultimate goal of modeling Hot Jupiter precession on a statistical scale.

8. Code Availability

The DE-MCMC orbital evolution fitting pipeline developed for this manuscript is publicly available on Zenodo (de Beurs 2023) and a living version is available on GitHub.¹⁵ The code was run on seven cores of an M1 Macbook Air (16 GB RAM).

Acknowledgments

Z.L.D. and J.B. would like to thank the generous support of the MIT Presidential Fellowship and to acknowledge that this material is based upon work supported by the National Science Foundation Graduate Research Fellowship under grant No. 1745302. Z.L.D. would like to acknowledge the MIT Collamore-Rogers Fellowship. Work by J.N.W. was supported by a NASA Keck PI Data Award.

This research has made use of the SIMBAD database and VizieR catalog access tool, operated at CDS, Strasbourg, France. This research has made use of NASA's Astrophysics Data System. This work has made use of data from the European Space Agency (ESA) mission Gaia (<https://www.cosmos.esa.int/gaia>), processed by the Gaia Data Processing and Analysis Consortium (DPAC, <https://www.cosmos.esa.int/web/gaia/dpac/consortium>). Funding for the DPAC has

been provided by national institutions, in particular the institutions participating in the Gaia Multilateral Agreement.

Appendix

In this appendix, we include the RV measurements included in this analysis (Table A1). In addition, we provide a supplemental figure of the expected RV measurements for each of the possible models during the next observing window (Figure A1). Lastly, we include more detailed descriptions of the performance metrics used in evaluating each of our models.

A.1 Performance Metrics

We use the loglikelihood, reduced chi-squared statistic, BIC, and AIC to evaluate the goodness of fit for our models. For completeness and pedagogical purposes, we include more detailed descriptions of each of these metrics here.

The loglikelihood ($\ln(L)$) is the natural log of the joint probability of the observations as a function of the parameters of the model. The likelihood is often written as $L(\theta|X)$ to emphasize that it is a function of the parameters θ given the data X . To find the most optimal θ given X , we sample a range of θ to maximize the likelihood. In practice, we do this by maximizing ($\ln(L)$) for practical purposes. In our case, the loglikelihood is defined as

$$\ln(L) = -\sum_i 0.5 * \frac{(x_i - \hat{x}_i)^2}{\sigma^2} + \ln(\sigma), \quad (\text{A1})$$

where x_i is the i th observation in x and σ is the estimated variance.

The reduced chi-squared statistic (χ_v^2) is one of the most widely used metrics to assess the goodness of fit. A lower χ_v^2 indicates a better fit to the data. The χ_v^2 is defined as

$$\chi_v^2 = \frac{1}{N-1} \sum_i \frac{(x_i - \hat{x}_i)^2}{\sigma^2}, \quad (\text{A2})$$

where N is the number of observations, k is the number of free parameters, x_i is the i th observation in x , \hat{x}_i is the model prediction for the i th observation, and σ is the estimated variance. In general, a $\chi_v^2 > 1$ corresponds to a model that does not fully capture the complexity of the data and that error variance has been underestimated. In a model where $\chi_v^2 \ll 1$, the model is overfitting and thus either (a) the error variance is overestimated or (b) the model is not properly fitting the noise in the observations. Generally, a χ_v^2 close to 1 corresponds to a proper fit and a lower value indicates a better fit to the data.

The BIC (Schwarz 1978) is based on the likelihood function and adds a penalty term to the number of parameters in the models to reduce overfitting. Models with a lower BIC are generally preferred. The BIC is defined as

$$\text{BIC} = k \ln(n) - 2 \ln(\hat{L}), \quad (\text{A3})$$

where \hat{L} is the maximized value of the likelihood function, n is the number of observations, and k is the number of free parameters in the model.

The AIC (Akaike 1974) also uses the likelihood function and is founded in information theory, where it estimates the relative amount of information lost by a given model. The better model is the model where less information is lost. AIC allows one to strike a balance between optimizing the goodness of fit and the

¹⁵ https://github.com/zdebeurs/Evolving_e_om_wobbling_edmcmc

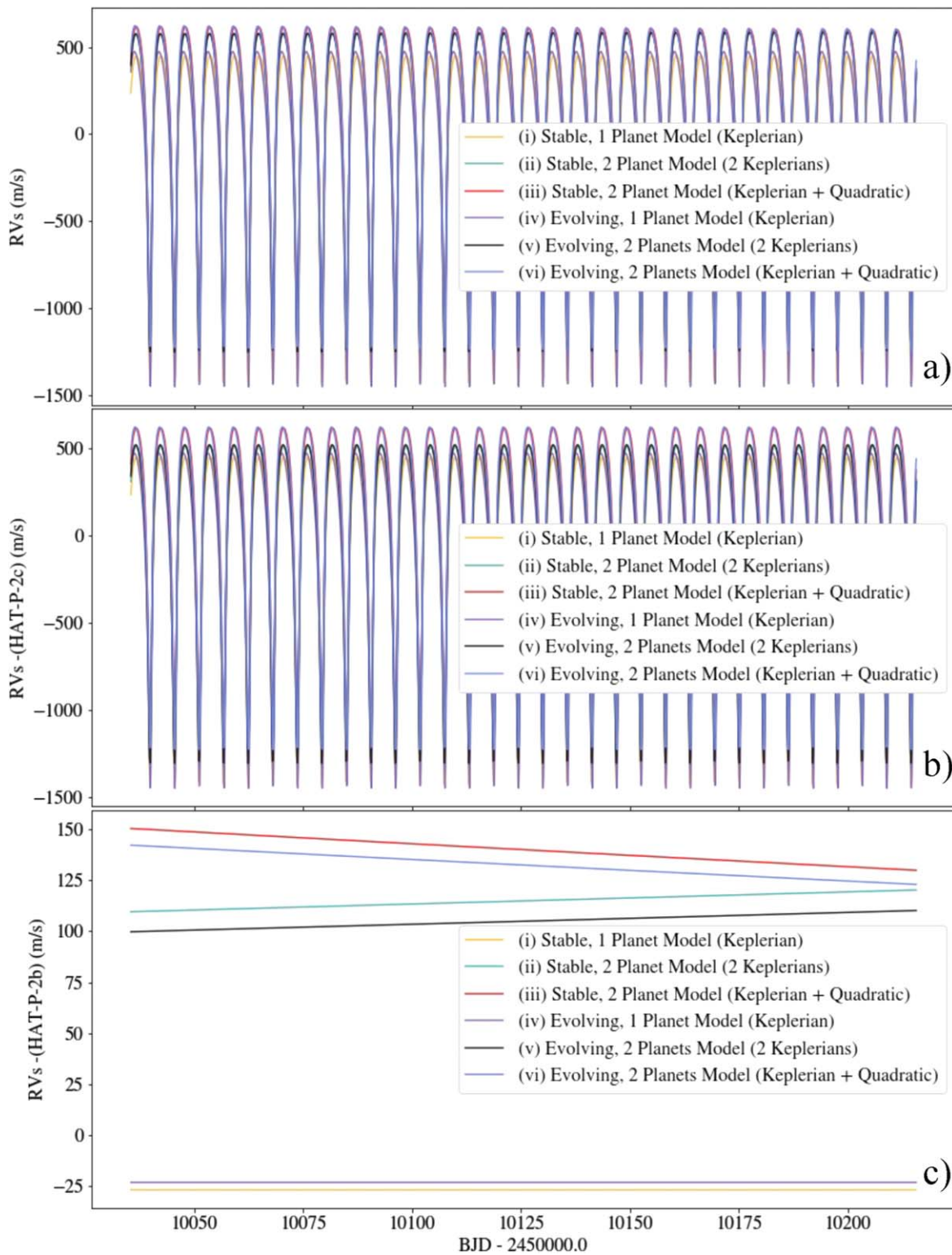


Figure A1. Expected RVs for each orbital model for the current observing window (2022 April 1–2023 September 28). (a) The expected RVs for the six orbital models from Table 1 are plotted for 32 orbits starting on 2022 April 1. (b) The expected RVs minus the long-period companion are plotted. (c) The expected RVs minus HAT-P-2 c are plotted.

Table A1
Summary of RV Measurements

BJD-2450000	Instrument	RV (m s ⁻¹)	σ_{RV}
3981.77824	HIRES	-30.10	7.78
3982.87244	HIRES	-324.11	7.00
3983.81561	HIRES	479.98	7.50
3984.89572	HIRES	826.89	7.31
4023.69226	HIRES	684.77	7.51
4186.99899	HIRES	648.04	7.82
4187.1049	HIRES	631.44	7.01
4187.16062	HIRES	654.71	7.01
4188.01763	HIRES	702.91	7.07
4188.16036	HIRES	721.16	6.89
4189.01112	HIRES	588.58	6.98
4189.08965	HIRES	595.95	6.90
4189.15846	HIRES	563.03	7.74
4216.96014	HIRES	660.49	8.42
4279.87763	HIRES	385.93	8.60
4285.8246	HIRES	109.99	5.58
.	.	.	.
.	.	.	.
7891.38229	HARPS-N	-237.31	3.64
7891.38885	HARPS-N	-127.17	3.62
7891.39284	HARPS-N	-191.79	3.33
7891.39647	HARPS-N	-180.93	3.36
7891.68477	HARPS-N	-617.71	3.24
7891.69311	HARPS-N	-594.11	1.86
7953.48534	HARPS-N	-218.48	1.21
7975.43735	HARPS-N	221.07	1.43
7989.35655	HARPS-N	541.67	1.31
8024.41654	HARPS-N	775.37	1.20
8263.12948	HIRES	-100.28	6.33
8386.70729	HIRES	208.80	6.09
8645.77618	HIRES	202.41	5.68
8648.8643	HIRES	586.11	6.54
8648.86713	HIRES	588.86	6.73
8648.86985	HIRES	594.18	6.21
9042.84334	HIRES	534.45	7.19
9092.71825	HIRES	58.63	7.35

Note. Full table available online.



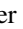

(This table is available in its entirety in machine-readable form.)





simplicity of the model. In this way, AIC allows one to deal with the problems of overfitting and underfitting the data. AIC is defined as

$$AIC = k - 2 \ln(\hat{L}), \quad (A4)$$

where the model with the lowest AIC value is the preferred model.

ORCID iDs

Zoë L. de Beurs  <https://orcid.org/0000-0002-7564-6047>
 Julien de Wit  <https://orcid.org/0000-0003-2415-2191>
 Alexander Venner  <https://orcid.org/0000-0002-8400-1646>
 David Berardo  <https://orcid.org/0000-0001-6298-412X>

Jared Bryan  <https://orcid.org/0000-0001-9466-1843>
 Joshua N. Winn  <https://orcid.org/0000-0002-4265-047X>
 Benjamin J. Fulton  <https://orcid.org/0000-0003-3504-5316>
 Andrew W. Howard  <https://orcid.org/0000-0001-8638-0320>

References

- Akaike, H. 1974, *ITAC*, **19**, 716
- Albrecht, S., Winn, J. N., Johnson, J. A., et al. 2012, *ApJ*, **757**, 18
- Becker, J. C., Vanderburg, A., Adams, F. C., Khain, T., & Bryan, M. 2017, *AJ*, **154**, 230
- Berardo, D., Crossfield, I. J. M., Werner, M., et al. 2019, *AJ*, **157**, 185
- Blunt, S., Endl, M., Weiss, L. M., et al. 2019, *AJ*, **158**, 181
- Bonomo, A. S., Desidera, S., Benatti, S., et al. 2017, *A&A*, **602**, A107
- Brandt, T. D. 2018, *ApJS*, **239**, 31
- Brandt, T. D. 2021, *ApJS*, **254**, 42
- Brandt, T. D., Dupuy, T. J., & Bowler, B. P. 2019, *AJ*, **158**, 140
- Cosentino, R., Lovis, C., Pepe, F., et al. 2012, *Proc. SPIE*, **8446**, 84461V
- Cowan, N. B., & Agol, E. 2011, *ApJ*, **726**, 82
- de Beurs, Z. L. 2023, wobble_edmdmc: Orbital Evolution RV Fitting Software, v1.0, Zenodo, doi:10.5281/zenodo.8161226
- de Wit, J., Lewis, N. K., Knutson, H. A., et al. 2017, *ApJL*, **836**, L17
- Deming, D., Knutson, H., Kammer, J., et al. 2015, *ApJ*, **805**, 132
- Eggleton, P. P., Kiseleva, L. G., & Hut, P. 1998, *ApJ*, **499**, 853
- Errico, A., Wittenmyer, R. A., Horner, J., et al. 2022, *AJ*, **163**, 273
- Fabrycky, D. C., & Winn, J. N. 2009, *ApJ*, **696**, 1230
- Fuller, J., & Lai, D. 2012, *MNRAS*, **420**, 3126
- Fulton, B. J., Petigura, E. A., Blunt, S., & Sinukoff, E. 2018, *PASP*, **130**, 044504
- Gelman, A., & Rubin, D. B. 1992, *StaSc*, **7**, 457
- Goodman, J., & Dickson, E. S. 1998, *ApJ*, **507**, 938
- Householder, A., & Weiss, L. 2022, arXiv:2212.06966
- Howard, A. W., Johnson, J. A., Marcy, G. W., et al. 2010, *ApJ*, **721**, 1467
- Hut, P. 1981, *A&A*, **99**, 126
- Ivshina, E. S., & Winn, J. N. 2022, *ApJS*, **259**, 62
- Jordán, A., & Bakos, G. Á. 2008, *ApJ*, **685**, 543
- Kipping, D. 2018, *RNAAS*, **2**, 223
- Knutson, H. A., Fulton, B. J., Montet, B. T., et al. 2014, *ApJ*, **785**, 126
- Levrard, B., Winisdoerffer, C., & Chabrier, G. 2009, *ApJL*, **692**, L9
- Lewis, N. K., Knutson, H. A., Showman, A. P., et al. 2013, *ApJ*, **766**, 95
- Lewis, N. K., Showman, A. P., Fortney, J. J., Knutson, H. A., & Marley, M. S. 2014, *ApJ*, **795**, 150
- Lin, D. N. C., Bodenheimer, P., & Richardson, D. C. 1996, *Natur*, **380**, 606
- Lin, D. N. C., & Ida, S. 1997, *ApJ*, **477**, 781
- Ma, L., & Fuller, J. 2021, *ApJ*, **918**, 16
- Mayor, M., & Queloz, D. 1995, *Natur*, **378**, 355
- Ment, K., Fischer, D. A., Bakos, G., Howard, A. W., & Isaacson, H. 2018, *AJ*, **156**, 213
- Paxton, B., Bildsten, L., Dotter, A., et al. 2011, *ApJS*, **192**, 3
- Rasio, F. A., & Ford, E. B. 1996, *Sci*, **274**, 954
- Salz, M., Schneider, P. C., Czesla, S., & Schmitt, J. H. M. M. 2016, *A&A*, **585**, L2
- Schwarz, G. 1978, *AnSta*, **6**, 461
- Ter Braak, C. J. F. 2006, *Statist. Comput.*, **16**, 239
- Townsend, R., Teitler, S., & Paxton, B. 2014, in IAU Symp. 301, Precision Asteroseismology, ed. J. A. Guzik et al. (Cambridge: Cambridge Univ. Press), 505
- Vanderburg, A., Becker, J. C., Kristiansen, M. H., et al. 2016, *ApJL*, **827**, L10
- Venner, A., Pearce, L. A., & Vanderburg, A. 2022, *MNRAS*, **516**, 3431
- Venner, A., Vanderburg, A., & Pearce, L. A. 2021, *AJ*, **162**, 12
- Vogt, S. S., Allen, S. L., Bigelow, B. C., et al. 1994, *Proc. SPIE*, **2198**, 362
- Weidenschilling, S. J., & Marzari, F. 1996, *Natur*, **384**, 619
- Winn, J. N., Johnson, J. A., Peek, K. M. G., et al. 2007, *ApJL*, **665**, L167
- Witte, M. G., & Savonije, G. J. 2002, *A&A*, **386**, 222